APPLIED RESEARCH

Continuous Terahertz Wave Imaging for Debonding Detection and Visualization Analysis in Layered Structures

KAILIANG XUE[1], YOUXING CHEN[1,2], WENNA ZHANG[1], JIALIN SONG[1], ZHAOBA WANG[1,2], YONG JIN[1,2], AND XIN GUO[1]

[1]School of Information and Communication Engineering, North University of China, Taiyuan 030051, China
[2]National Key Laboratory for Electronic Measurement Technology, North University of China, Taiyuan 030051, China

Corresponding author: Youxing Chen (chenyouxing@nuc.edu.cn)

ABSTRACT Continuous terahertz detection imaging technology is widely used in polymer detection. However, it is very difficult to quantitatively analyze defects due to the characteristics of focusing lenses. On the one hand, a lens with a short focal length means the achievement of a better spatial resolution and a poor depth resolution. On the other hand, a lens with a long focal length results in a better depth resolution and a worse spatial resolution. In addition, in order to ensure the positioning accuracy, the upper surface of a sample is often used as the focal plane for detection, which causes the energy outside the range of the focal depth to drastically decrease and seriously affect the imaging quality. In this paper, a method is proposed for debonding detection and quantitative analysis in layered structures. Firstly, by using multi-directional structural elements for measuring the difference between the debonding region and local surroundings, we extract defective edges and suppress clutters by establishing a multi-directional morphological filter. Then, the improved Otsu method is used for threshold segmentation and the population mean entropy is used to calculate the optimal threshold. Finally, the superiority of the proposed method is confirmed on synthetic datasets with low SNR images, and it is successfully applied to terahertz image processing. Moreover, the results of the proposed algorithm show that the debonding region detection error of the terahertz image is controlled within 10.17%-11.27%. It provides a new method and idea for quantitative analysis of terahertz detection in layered structures.

INDEX TERMS Terahertz FMCW, non-destructive testing, mathematical morphology, edge detection.

I. INTRODUCTION

Because of having high hardness, high temperature resistance and corrosion resistance, ceramic matrix composites (CMC) are often used as an important part of thermal protection structures (TPS), especially in the aerospace field [1], [2], [3]. The production process of TPS involves the bonding of CMC, insulation felt and protected structure in turn through adhesives. The final TPS is made in the order of CMC/glue layer 1/insulation felt/glue layer 2/protected structure from outside to inside [4]. Due to the influences of

the production process and service environment, the position of the TPS surface gets easily debonded, which causes great security risks. So, it is very necessary to use some non-destructive testing (NDT) methods for detecting bonding conditions. The thickness of CMC in TPS is generally 25 mm - 40 mm [5]. Its porous and loose properties limit the use of traditional NDT methods. With the rapid development of terahertz radiation and detection technology, terahertz NDT has drawn huge attention in recent years.

In fact, the terahertz band is a very special band, which lies between infrared light and millimeter waves. The terahertz wave can irradiate optically opaque dielectric materials with certain penetration and reflection ability [6], [7], [8],

The associate editor coordinating the review of this manuscript and approving it for publication was S. M. Abdur Razzak.

[9], [10], [11], [12]. It has good spatial resolution also. Therefore, it is widely used in safety inspection [13], [14], wireless communication [15], nondestructive testing [16], [17], biomedicine field [18], [19], and so on. More specifically, terahertz NDT provides effective results in the health monitoring of composite materials and inspection of layered structures [20], [21],with Time-domain Spectroscopy (TDS) techniques and Frequency Modulated Continuous Wave (FMCW) radars.

The FMCW sensing is more suitable for fast imaging due to its high integration, short measurement time and strong robustness [22]. The imaging process of FMCW can be performed through synthetic aperture imaging or real-aperture imaging. With low energy aggregation and large beam attenuation in free space, the former is often used in security inspection [14]. It is not suitable for NDT in cases where higher scanning accuracy is required. In contrast, the latter (real-aperture imaging) can obtain more concentrated energy and the best echo signal by using a set of optical collimating lenses for focusing the antenna radiation beam on the region of interest [21]. A shorter focal length means the achievement of a better focusing performance, more concentrated energy, a smaller focusing spot diameter, and more accurate lateral resolution [22], [23], [24], [25]. But it also has drawbacks. There is no doubt that a lens with a short focal length has a short focal depth. It is found that with the influence of the characteristics of optical lens, the energy outside the range of the focal depth shows a nonlinear cliff attenuation, which directly leads to a sharp decline in deep detection. Hence, the spectral peak of the debond layer signal (DLS) near the bottom layer is not much different from the adhere layer signal (ALS), even if it may go below ALS. Although a lens with a long focal length can ensure deeper inspection, its large diameter spot is not friendly to small-size defects. Therefore, it is of great significance to perform quantitative analysis for accurately extracting the debonding region in FMCW detection by using a lens with a short focal lens. This is also the main problem solved in this paper.

Some significant research achievements in FMCW signal processing have been reported in the literature. Dai et al. [5] proposed a wavelet transform for processing 3D data of FMCW detection, and reconstructed a 3D structure by using a wavelet coefficient. Hu et al. [27] proposed a method for reconstructing the range profile by integrating the super-resolution capacity of the MUSIC algorithm with a data fitting method. High-resolution spectral estimation techniques, such as the model-based signal processing technique [28], state-space algorithms [29], and matrix pencil method [30], have also been reported to be effective in FMCW detection. Although all these methods process a single echo signal for obtaining a higher depth resolution, they ignore the changes in the echo signal between two adjacent sampling positions. The quantitative analysis of defects is poor. In order to overcome the interference of ALS on the weak target detection in the debonding region, we propose a new method, taking TPS as the research

object, for the purpose of debond detection and quantitative analysis in a layered polymer. Initially, the multi-directional structural elements are designed by analyzing the peak distribution of the echo spectrum on the bonding layer for sensing the edge of the debonding region. Combined with the morphological method, the difference between the edge of the debonding region and local surroundings can be measured from the directional morphological filters. Then, according to the consistently low reflection level shown by the edge of defect in a certain direction, an improved Otsu method is proposed for distinguishing the target from the strong structure clutters. Finally, the effectiveness of the proposed method is demonstrated through comparative experiments. The debonding region can be well extracted by using the above method, which is meaningful for the FMCW NTD method.

The remaining part of this paper is organized as follows: The characteristics and detection problems of the debonding layer region are discussed in Section II. Section III presents the details of the proposed detection method combined with the morphological processing and improved Otsu method. Subsequently, the effectiveness of the proposed method in low SNR images and the analysis of detection errors in FMCW images are presented and discussed in Section IV. Finally, the conclusions of the present work are drawn in Section V.

II. PRELIMINARIES
This part mainly introduces the architecture and detection principle of FMCW radar. By analyzing the TPS detection signals, the existing problems are put forward.

A. PRINCIPLE OF FMCW RADAR DETECTION
The FMCW detection system used in this study is a reflective imaging system based on electronic excitation. The technology for continuous wave generation and frequency mixing detection has made some progress, focusing mainly on Si-based fully devices [31] and high frequency precision radars [32]. Although different frequency doubling links can excite continuous waves of different frequency bands, all of them are implemented based on similar architectures. Figure 1 shows the basic architecture of the terahertz detection system and the principle of FMCW measurement. In terms of signal generation, a ramp generator drives a voltage control oscillator (VCO) combined with a Phase Locked Loop (PLL) for generating the fast saw tooth low-frequency sweep signal. The low-frequency sweep signal is amplified by a frequency multiplier for using as the transmitted signal (TX) of the terahertz system, part of which is radiated into the air by the antenna. Finally, the major part of the energy is concentrated in a focal plane through a set of focusing lenses. When the focused signal encounters the layers bonded by different materials, it is returned to the terahertz source through the same path as the reflected signal (RX). Other parts of both TX and RX go to the mixer, where
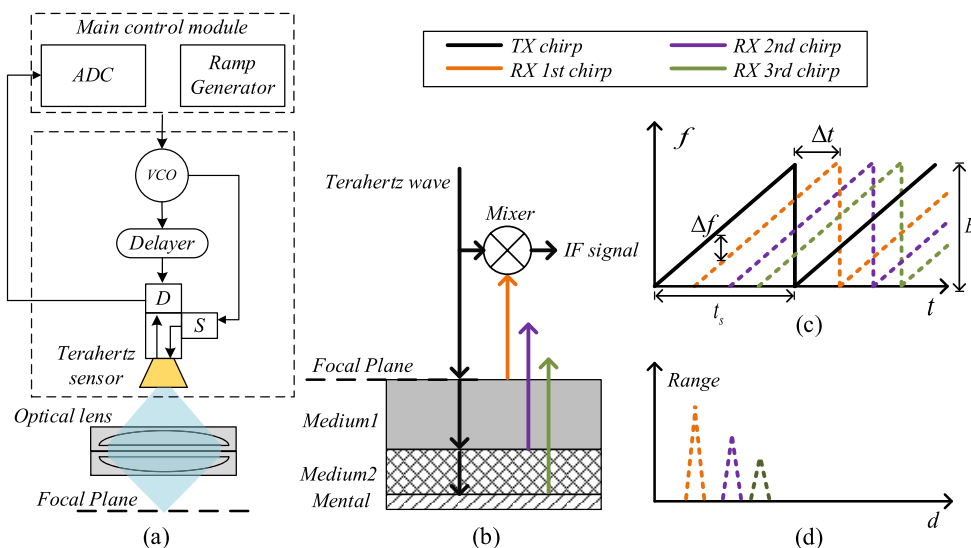
FIGURE 1. The basic architecture of terahertz detection system and the principle of FMCW measurement. (a) Structure composition and operating principle. (b) Schematic diagram of a typical layered (two-layer) structure with TX and RX transmission paths. (c) Sensing scheme for FMCW measurement. (d) Range profiles from FFT spectral information of IF signals.

they are eventually recorded by ADC as the intermediate frequency (IF) signal.

The measurement principle and signal analysis model of a typical layered (two-layer) structure are shown in Fig.1(b)-1(d). The RX chirp can be regarded as a delayed signal of the TX chirp, and the frequency of RX increases linearly with that delay time. The TX chirp can be expressed as follows:

$$S_{TX}(t) = A_t \exp\left[j2\pi\left(f_0 t + \frac{1}{2}Kt^2\right)\right] \quad (1)$$

where A_t is the amplitude of TX, f_0 is the initial frequency, B is the system bandwidth, K is the chirp rate that can be represented by B/t_s, and t_s is the sweep time. When the FMCW sensing is used for detecting the layered structures, the RX chirp reflected from different interface layers corresponds to different delay times, which gradually increase with increasing distance.

Meanwhile, the amplitude of the RX chirp is affected by the characteristics of a sample. The RX chirp can be expressed as follows:

$$S_{RX}(t) = A_r \exp\left\{j2\pi\left[f_0(t-\Delta t) + \frac{1}{2}K(t-\Delta t)^2\right]\right\} \quad (2)$$

where A_r is the amplitude of RX. For the FMCW radar, the captured raw data shows the RX chirp as a summation of the cosine function of different frequencies, where the frequency components correspond to the beat frequency Δf of the respective reflection with the time shift Δt. Taking the first RX chirp as an example, the intermediate frequency (IF) signal can be expressed as:

$$S_{IF}(t) = \frac{A_t A_r}{2} \exp\left[j2\pi\left(tK\Delta t + f_0\Delta t - \frac{1}{2}K\Delta t^2\right)\right] \quad (3)$$

Combining the relationship between distanced d and time shift Δt, the beat frequency Δf can be obtained by FFT as expressed as follows:

$$\Delta f = \frac{2nBd}{t_s c} \quad (4)$$

where c is the speed of light, and n is the refractive index of the material ($n = 1$ in the air). Then, distance d can easily be calculated as follows:

$$d = \frac{ct_s \Delta f}{2nB} \quad (5)$$

According to the information carried by the IF signal, the defect visualization can be characterized by intensity, phase, distance, etc. The sampling point and sampling rate should also be considered in the actual detection.

B. PROBLEM ANALYSIS

We use a reflective FMCW imaging system with a set of optical focusing lenses for the detection experiment, which is a two-dimensional scanning system that operates at 126-182 GHz. The sweep time t_s of the system is 1.024 ms, and the ADC sampling rate is 1 MHz. According to the diffraction limit formula, the minimum imaging resolution of the proposed system is about 2.4 mm. The experimental data were acquired using this device.

Similar to infrared imaging, FMCW detection imaging is performed by measuring the terahertz waves reflected by objects, then mixing frequencies and extracting feature quantity for imaging. The outcome of this imaging is a typical discrete image, whose grayscale distribution has no linear relationship with the reflection characteristics of the detected object. Figure 2 shows the histogram and fitting curve of the signal strength distribution at a typical bonding interface,
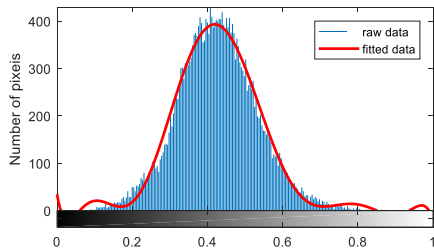
FIGURE 2. Histogram and fitting curve of signal intensity distribution at a bonding interface.
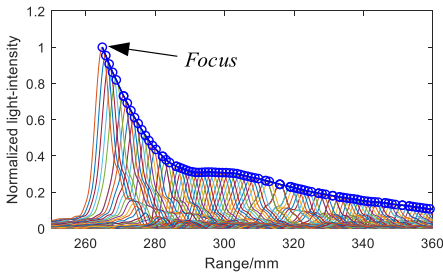
FIGURE 3. Signals measured outside the focus range of a 50 mm lens.
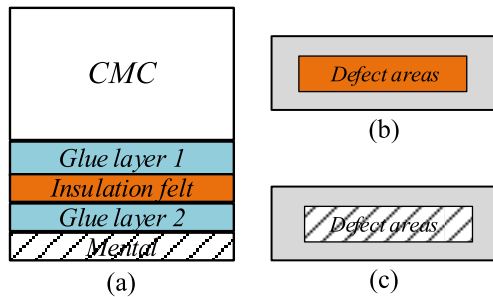
FIGURE 4. TPS structure. (a) Order of thickness in each layer is 35 mm/ 0.2 mm / 2 mm / 0.2 mm / 3 mm from top to bottom. (b) Sample 1 with the debonding region in glue layer 1. (c) Sample 2 with the debonding region in glue layer 2.

where it can be seen easily that the distribution approximately matches the Gaussian distribution.

According to the theoretical analysis and experimental test, the terahertz wave attenuates greatly when it propagates in the air. Although a lens with a short-focal length can capture better energy at the focal point and maintain a certain focal depth, it is more noteworthy that the energy outside the range of the focal depth shows a sharp decline. The signals measured outside the focus range of the 50 mm lens are shown in Fig. 3. At about 30-35 mm outside the focal plane, only about 35 percent of the energy remains, and even lower than that when the attenuation characteristics of the materials are considered. There is no doubt that the DLS will be submerged in ALS, resulting in a low SNR image and an increase in false targets, which will cause great obstruction to visualization.

The TPS used in this experiment is shown in Fig. 4, whose debonding glue layer is filled with dry glue of various sizes and shapes as defects. The specimen with defects in glue layer 1 is labeled as the sample 1 as shown in Fig. 4(b), and the specimen with defects in glue layer 2 is labeled

as the sample 2 as shown in Fig. 4(c). Figure 5 shows the FMCW imaging results and typical signals of different positions. Due to the influence of the bonding process, the roughness of the adhesive interface has a great influence on the echo signal, and the fault-free position also shows energy fluctuation.

Limited by the system bandwidth, it is not easy to directly distinguish the interface echo of glue layer 1/insulation felt and insulation felt/glue layer 2, but the features can still be extracted from the inflection points of signals. Due to the presence of air layer in the debonding part, the terahertz waves are scattered in different directions, which causes the spectral peak of DLS to rise and fall, making it difficult to distinguish from ALS. However, at the edge of the debonding part, its connectivity and the signal mutation of adjacent positions provide ideas for signal characterization (see Fig. 6) as follows:

① Due to the closed-loop characteristics and influence of absolute scattering, the edge of the defect maintains a low level of energy reflection along a certain direction, which helps us to enhance the differential features.

② Defective edges show similar characteristics in the outer normal direction. In other words, the difference of the gray gradient between the defective edge and the outer normal direction ALS is similar, which can be used to further suppress the strong clutter.

In conclusion, these concepts are used in designing the edge detection filter that can accurately extract contour information in low SNR imaging data.

III. PROPOSED METHOD

The morphological processing method is one of the commonly used algorithms for detecting the edges of images. In this section, we first introduce the basic principle of morphological filtering. Then, according to the characteristics of an FMCW image, its multi-directional structural elements are constructed to perceive its edge details. Combined with the morphological operation, an adaptive weight fusion filter is designed for measuring the multi-directional differences between the defect and local surroundings. Finally, an image with a clear edge profile can be obtained by using threshold segmentation processing through the improved Otsu method.

A. CLASSICAL MATHEMATICAL MORPHOLOGY

Mathematical morphology, based on the set theory, is an effective nonlinear tool in image processing. Its basic concept is to detect the profile of a defect by constructing various structural elements, and finally to get the image that retains more edge details. In mathematical morphology, $f(x, y)$ is defined as the FMCW image, and $B(u, v)$ as its structural element. Its two fundamental operators can be given by the following formula:

$$f(x, y) \ominus B(u, v) = \min \{f(x - u, y - v) - B(u, v)\} \quad (6)$$
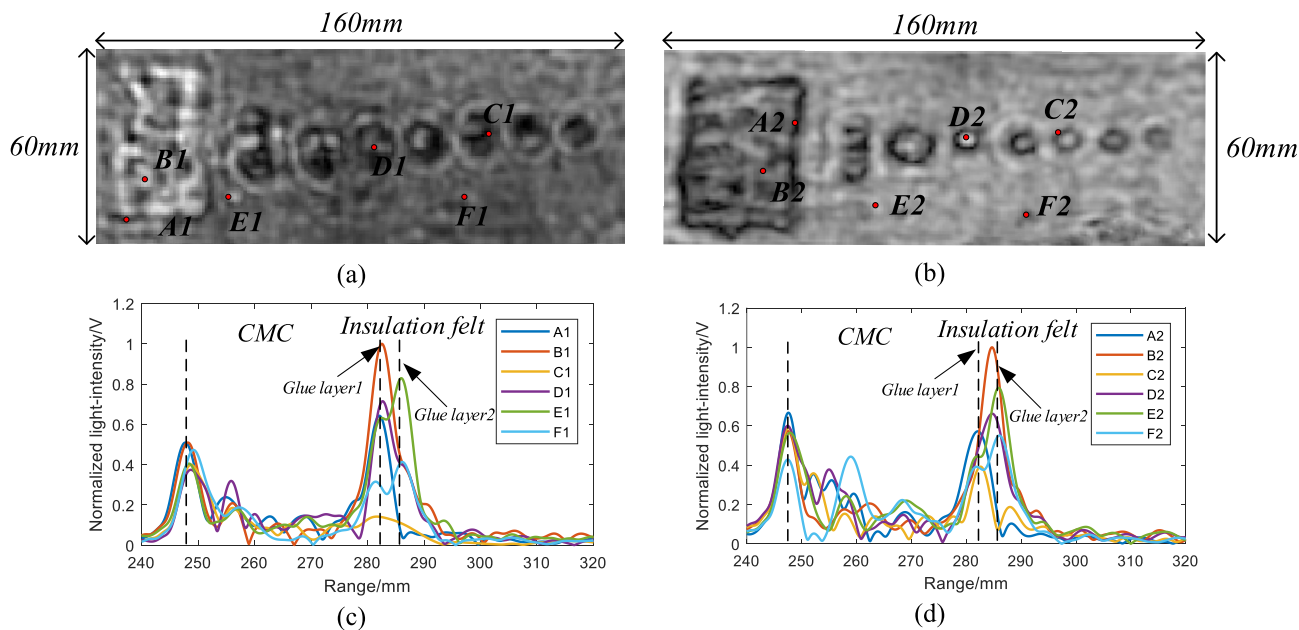$$f(x, y) \oplus B(u, v) = \max \{f(x - u, y - v) + B(u, v)\} \quad (7)$$

FIGURE 5. Imaging results and characteristics of dimensional range. (a-b) Represent imaging results characterized by the FFT spectral peak of glue layer 1 and glue layer 2 as the characteristic quantities. (c-d) Typical signals of different positions, where A-D represent signals of DLS, and E-F represent signals of ALS.
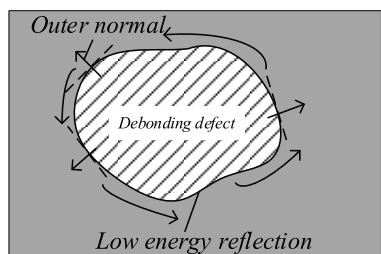

FIGURE 6. Schematic of a typical debonding defect.

FIGURE 7. Relationship between structural elements of NWTH and NBTH.

where (x, y) and (u, v) represent two pixels coordinates; Θ and $\oplus$ are the corrosion and expansion operators, respectively. Then, the corrosion needs to obtain a darker image by using a domain-wide minimum operator method. In contrast, the expansion operation uses a domain-wide maximum operator method to obtain a brighter image. On the basis of the above formulas, two operations can be derived: the morphological opening $\circ$ and closing $\bullet$ operators, which can be defined as follows:

$$f \circ B = (f \Theta B) \oplus B \tag{8}$$

$$f \bullet B = (f \oplus B) \Theta B \tag{9}$$

These basic operations optimize the detail and target population. In a target detection scene, the classical top-hat and bottom-hat filters are often used to highlight the bright and dark areas, respectively. However, for the images with low SNR, the effect of detection is drastically decreased. For small target detection, Bai and Zhou [33] proposed two new filters, $NWTH$ and $NBTH$, which can be expressed in formulas
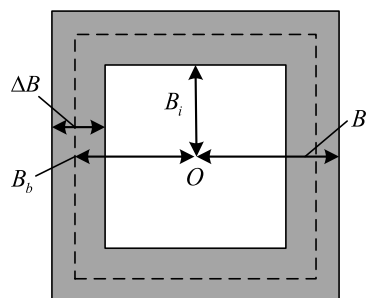
as follows:

$$NWTH(x, y) = f(x, y) - f * B_{oi} \tag{10}$$

$$NBTH(x, y) = f \otimes B_{oi}(x, y) - f(x, y) \tag{11}$$

where B_{oi} represents the two selected elements B_o and B_i. The operations $f * B_{oi}$ and $f \otimes B_{oi}$ can be defined as:

$$f * B_{oi}(x, y) = (f \oplus \Delta B) \Theta B_b(x, y) \tag{12}$$

$$f \otimes B_{oi}(x, y) = (f \Theta \Delta B) \oplus B_b(x, y) \tag{13}$$

where B_b represents an element of size between B_o and B_i, and $\Delta B = B_o - B_i$. Specifically, the relationship between them is shown in Fig.7, where the point O represents the center of the structural element. For $NWTH$, $f * B_{oi}$ adopts an operation of expansion before corrosion. The expansion operator removes the negative noise by replacing all the pixels in the target area with the maximum gray value of surrounding area ΔB; while the corrosion operator replaces area B_b with the minimum gray value of that surrounding
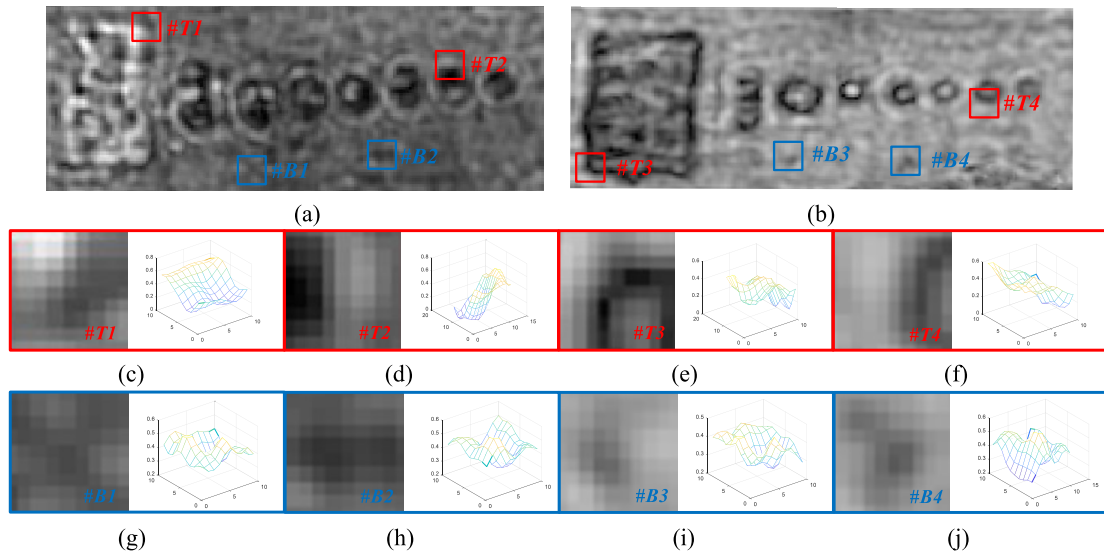
FIGURE 8. FMCW imaging results and image blocks of typical areas. (a) FMCW image of sample 1. (b) FMCW image of sample 2. (c) - (f) Image blocks of typical defective areas of some typical directions. (g) - (j) Background clutters.
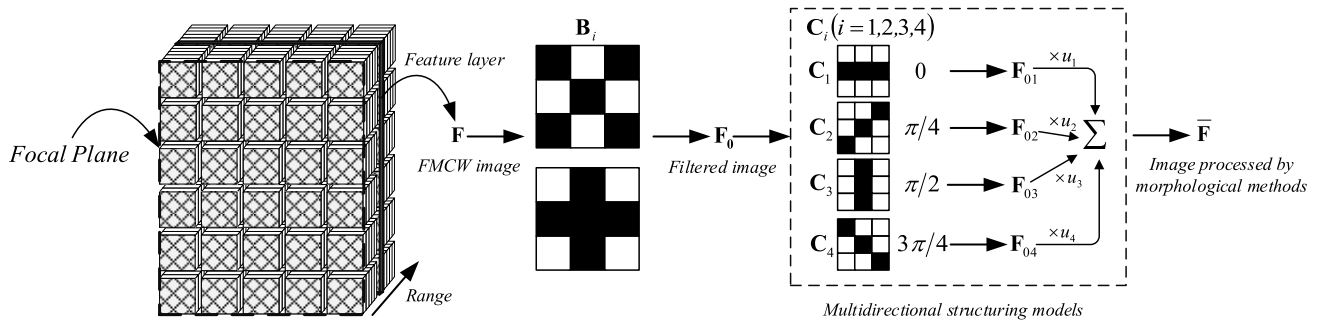

FIGURE 9. Block diagram of multi-directional morphological processing algorithm.

area, which can remove a part of the positive noise. Compared with the traditional top-hat filter, *NWTH* can extract the bright area without introducing too many background areas, resulting in better target detection. The same goes for the case of *NBTH* also. But these filters above are more suitable for the detection of small-point target with a light center and a dark periphery.

However, when detecting targets in strong clutters, strong clutters cause them to loss real targets or greatly increases the false targets, which are difficult to distinguish. Considering the directional difference between the edge and background, multi-directional structural elements are constructed for measuring the difference between the defect and local region of the inner and outer normal vectors.

B. MULTI-DIRECTIONAL MORPHOLOGICAL PROCESSING

A structural element plays an extremely important role in morphological filtering methods, which can be used as a probe to sense areas of interest. The background clutter can be removed by sliding structural elements. The selection of structural elements has a great influence on the processing of images. How to select appropriate structural elements

according to the requirement is one of the difficult problems in the field of mathematical morphology. The FMCW imaging results and image blocks of typical areas are shown in Fig. 8, where (a) - (b) are the FMCW images of sample 1 and sample 2, (T1) - (T4) are the edges of the debonding region in different directions, and (B1) - (B4) are the strong clutter regions. (c) - (f) directly reflect the fluctuation in the gray values of the defective edges observed from different directions, which is more obvious in the gradient direction. (g) - (j) show typical stationary or non-stationary background clutters. Although these clutter noises are similar to the defective edge in some directions, more importantly, they are dense areas with a few pixels having the size smaller than the Rayleigh limit of the system itself. So, it cannot be judged as a defect.

Based on the directional difference between the defect and local background, the morphological processing method of multi-directional structural elements is proposed. Figure 9 shows the block diagram of the algorithm. Firstly, B_i $(i = 1, 2)$ are the structural elements used in the pre-processing process (see Fig. 9), which can smooth the initial image. The black cell represents an active

structural element with the value of 1, and the white cell represents the inactive area filled with the value of 0. The smoothing filter can be given by the following formula:

$$f_0(x, y) = \frac{\sum_{i=1}^{2} [f \circ B_i \bullet B_{3-i}(x, y)]}{2} \qquad (14)$$

where $\bar{f_0}(x, y)$ is the pre-processed image. Then, the directional structural elements C_i ($i = 1, 2, 3, 4$) (see Fig.9) are constructed for extracting features from the multi-directional edge. The designed multi-directional morphological filter can be derived as follows:

$$\bar{f}(x, y) = \sum_{i=1}^{4} u_i \{f_0 \oplus C_i(x, y) - f_0 \Theta C_i(x, y)\} \qquad (15)$$

where $\bar{f}(x, y)$ represents the weighted sum of morphological processing results in different directions, and u_i is the weight. When edge detection algorithms deal with multi-direction and multi-scale detection problems, weighted average or manual parameter adjustment is often used in image fusion. However, due to the variation in the details of the target edge in different directions, a traditional weight selection method has low applicability and poor effect.

In mathematical morphology, the edge of an image can be determined by using the difference in the gray values obtained upon processing the image f_{0i} ($i = 1, 2, 3, 4$) (see Fig. 9) by a structural element in a certain direction. The larger the difference, the greater the probability that there are edge details in the normal vector of that structural element. In this way, it is possible to use the sum of the gray difference of f_{0i} ($i = 1, 2, 3, 4$) as the basis for adaptive weight adjustment. Figure 10 shows a 3×3 image area, where p_5 represents the

P_1	P_2	P_3
P_4	P_5	P_6
P_7	P_8	P_9

FIGURE 10. A 3 × 3 image area.

pixel value of the center point, and the difference in the gray value can be defined as:

$$h_i = |p_i - p_5|, i = 1, 2, \ldots, 9 \qquad (16)$$

The sum T_i ($i = 1, 2, 3, 4$) in each direction can be expressed as follows:

$$\begin{cases} T_1 = \sum_{i=1}^{3} (h_i + h_{10-i}) \\ T_2 = \sum_{i=0}^{2} (h_{2i} + h_{10-2i}) \\ T_3 = \sum_{i=0}^{2} (h_{3i+1} + h_{3i+3}) \\ T_4 = \sum_{i=1}^{3} (h_{i+1} + h_{9-i}) \end{cases} \qquad (17)$$

Finally, the weight can be given by the following formula:

$$u_i = \frac{T_i}{\sum_{i=1}^{4} T_i} \qquad (18)$$

The results of the proposed multi-directional edge detection (MDED) algorithm are shown in Fig. 11. The proposed algorithm first uses a set of small structural elements to filter the image, aiming to smooth the edge details and remove the detail points with sharp changes in light and dark. Then, considering the expanded direction of the defective profile, the multi-directional structural elements are constructed for extracting the details of the image, so that the edge can be effectively maintained and the strong clutters can be eliminated.

By using the morphological method, the noise reduction and edge extraction can be carried out for the imaging system $f(x, y)$. But the strong clutter background is preserved at the same time. From the results of the MDED and defect characteristics ① and ②, it can be seen that the defective edge still keeps a prominent pixel value and maintains in a certain direction, while the clutters show a low level and disorder. Therefore, the improved Otsu method is proposed for filtering the textured background while preserving the edge.
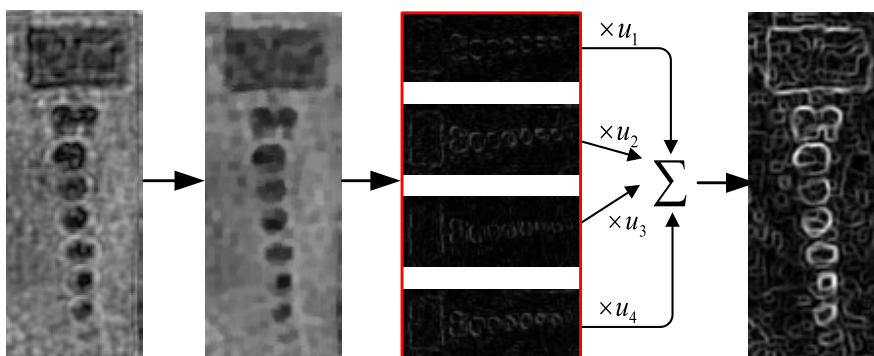

FIGURE 11. Results of the proposed multi-directional image processing (Sample 1).

C. IMPROVED OTSU METHOD

The Otsu method is a threshold segmentation algorithm that selects the maximum between-cluster variance of the target and local surroundings as the threshold selection criterion. Combining the characteristics of the targets and clutters, the optimal threshold is calculated by estimating the population mean.

Firstly, the gray level of image $\bar{f}(x, y)$ is set as L, and the gray value n of a pixel is set within $n \in (0, L)$. $p'(x, y)$ and $p''(x, y)$ represents the mean gray difference of a pixel in four and eight directions, respectively, which can be respectively given by the following formulas:

$$p'(x, y) = \frac{1}{4} \sum_{i=1}^{4} h_{2i} \tag{19}$$

$$p''(x, y) = \frac{1}{8} \sum_{i=1}^{8} h_i \tag{20}$$

where, $p'(x, y)$ and $p''(x, y)$ are defined as two new binary groups, whose occurrence time is represented by $X_{p'p''}$. Then, its two-dimensional joint probability density can be indicated as:

$$Y_{p',p''} = \frac{X_{p',p''}}{\text{size} \to \bar{f}(x, y)} \tag{21}$$

where $\text{size} \to \bar{f}(x, y)$ is the total number of pixels in the image $\bar{f}(x, y)$. The probability of defective edges and clutters can be expressed as follows:

$$\omega_{\text{defect}} = \sum_{p'=1}^{a_0} \sum_{p''=1}^{a_1} Y_{p',p''} \tag{22}$$

$$\omega_{\text{noise}} = \sum_{p'=a_0+1}^{L} \sum_{p''=a_1+1}^{L} Y_{p',p''} \tag{23}$$

where (a_0, a_1) is the threshold range. It can be concluded that the corresponding mean vector can be expressed as follows:

$$\boldsymbol{\mu}_{\text{defect}} = \left[\frac{\mu_{p'}}{\omega_{\text{defect}}}, \frac{\mu_{p''}}{\omega_{\text{defect}}} \right]^T$$
$$= \left[\frac{\sum_{p'=1}^{a_0} \sum_{p''=1}^{a_1} p' Y_{p',p''}}{\omega_{\text{defect}}}, \frac{\sum_{p'=1}^{a_0} \sum_{p''=1}^{a_1} p'' Y_{p',p''}}{\omega_{\text{defect}}} \right]^T \tag{24}$$

$$\boldsymbol{\mu}_{\text{noise}}$$
$$= \left[\frac{\sum_{p'=a_0+1}^{L} \sum_{p''=a_1+1}^{L} p' Y_{p',p''}}{\omega_{\text{noise}}}, \frac{\sum_{p'=a_0+1}^{L} \sum_{p''=a_1+1}^{L} p'' Y_{p',p''}}{\omega_{\text{noise}}} \right]^T \tag{25}$$

The population mean vector can be expressed as follows:

$$\boldsymbol{\mu}_L = [\mu_{\text{Ldefect}}, \mu_{\text{Lnoise}}]^T$$
$$= \left[\sum_{p'=1}^{L} \sum_{p''=1}^{L} p' Y_{p',p''}, \sum_{p'=1}^{L} \sum_{p''=1}^{L} p'' Y_{p',p''} \right]^T \tag{26}$$

The above equation can be transformed through an inter-class scatter matrix, and then the final optimized inter-class

variance can be expressed as follows:

$$K = \frac{\left(\mu_{\text{Ldefect}} \omega_{\text{defect}} - \mu_{p'}\right)^2 + \left(\mu_{\text{Lnoise}} \omega_{\text{defect}} - \mu_{p''}\right)^2}{\omega_{\text{defect}} \omega_{\text{noise}}} \tag{27}$$

When K reaches the maximum value, the image segmentation effect becomes the best, with (a_0, a_1) as the range of the corresponding threshold. In this paper, a_0 is selected as the optimal threshold. The final image is shown in Fig. 12, where the outline of the debonding region can be seen clearly, which provides an idea and method for the quantitative analysis of layered structure with debonding defect.

IV. EXPERIMENTS

In this section, we present the comparative experiments and detection error analysis of TPS. The superiority of the proposed method for the edge detection in low SNR images is verified by both subjective and objective evaluation.

A. EXPERIMENT SETTINGS

1) CONTRAST EXPERIMENT DETAILS

Since it is very difficult to obtain a large number of FMCW images and corresponding noise-free FMCW images in the real world, the synthesized images are used for evaluating the proposed MDED algorithm. The synthesized images from the BSD500 dataset are used to evaluate the proposed algorithm. The synthesized images include both clean images and corresponding images with different Gaussian noise values. The selection basis of the Gaussian noise is shown in Fig. 2. We compare the proposed MDED algorithm with three traditional methods, namely Sobel [34], Prewitt [35], and Roberts [36], and four learning methods, namely DexiNed [37], HED [38], PiDiNet [39], and RINDNet [40]. The experiments were performed on a computer with 4.01GHz i7-6700K CPU and 32 GB RAM, and the training process was performed on an Nvidia 1080Ti GPU.

2) TERAHERTZ DATA PREPROCESSING AND IMAGING

The complete setup of our scanning equipment includes the terahertz wave sensor, three linear actuators, a data acquisition system and a touch screen monitor. The radar sensor is placed on the X-axis rail above the scanning plate. For the acquired raw time-domain data, we need
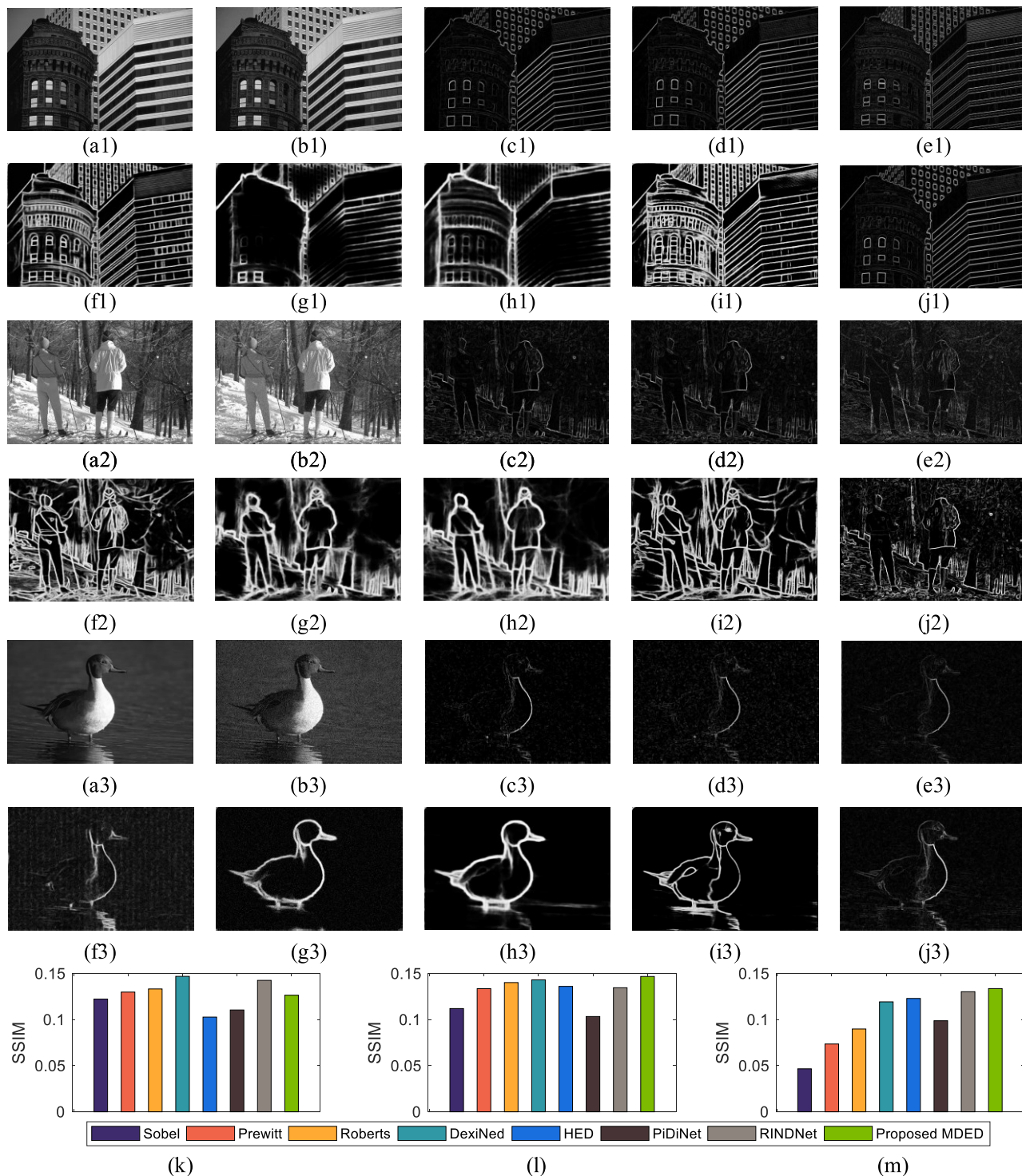
FIGURE 13. Comparison of visual effects of various methods on synthetic images. (a1-a3) O riginal image. (b1-b3) Images with 0.1%, 0.5%, and 1% Gaussian noise. (c1-c3) Results by Sobel. (d1-d3) Results by Prewitt. (e1-e3) Results by Roberts. (f1-f3) Results by DexiNed. (g1-g3) Results by HED. (h1-h3) Results by PiDiNet. (i1-i3) Results by RINDNet. (j1-j3) Results by Proposed MDED. (k-m) Bar charts of the corresponding SSIM.

to add a hamming window to achieve a better FFT effect. The measurement error in the range profile can be reduced by zero filling and nonlinear frequency modulation correction.

3) QUALITY MEASURES

In order to evaluate the performances of different methods for edge detection in noisy images, we apply a frequent measure, namely the structural similar index (SSIM). On the

other hand, since any real noise-free FMCW image cannot be obtained, the difference between the measured debonding region and the real region is used to illustrate the effectiveness.

B. EFFECTIVENESS OF SYNTHETIC DATASETS

Figure 13 shows the edge detection results for typical noisy images by different algorithms. The test images are buildings, people, and animals. The added noise is the Gaussian noise, the mean of which is 0, and the variance values are 0.1%, 0.5%, and 1%. It is easy to see that for images with high SNR levels, the traditional methods and deep learning methods can extract nearly the complete contour information (see Fig. 13 (a1 - h1, k)). However, as the SNR level decreases, a lot of edge details are lost. The superiority of the proposed MDED algorithm gradually manifests itself (see Fig.13 (a2 - h2, l)). When the noise is 1%, the

FIGURE 14. SSIM processed by different methods for a typical image with different SNR levels.

traditional methods cannot detect the complete edge, and the performances of the deep learning methods become poor. Although the HED and PiDiNet methods are able to detect large-size contours, details, such as reflections in the water, duck's eyes and so on, are lost. Similarly, the RINDNet method loses a small amount of tail and wing details (see Fig. 13 (a3 - h3, m)). Compared with other methods, the results of the proposed MDED method become more complete by removing the most noise and reserving the details of the target simultaneously. Especially, for a low SNR image, the effect is more obvious.

In order to reflect the ability of edge detection more directly in low SNR images, SSIM of images with different SNR levels is shown in Fig. 14. When the added noise level exceeds approximately 0.7%, the advantage of the proposed algorithm gradually increases.
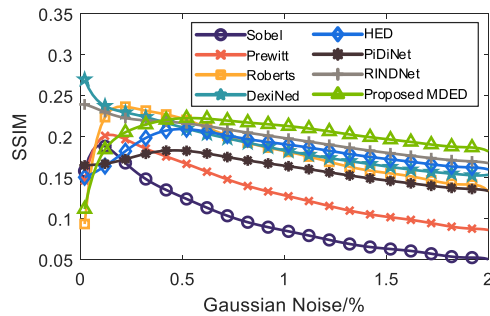
C. EFFECTIVENESS OF FMCW IMAGES

An FMCW image is an extremely low SNR image. Most methods always preserve strong clutters or shadow areas while extracting the edges, so it is impossible to conduct quantitative analysis. In contrast, in this paper, the combined method of MDED and improved Otsu can perform quantitative analysis. The final detection results are shown in Fig. 15. And defects are labeled I-VIII from left to right. The detection error is defined as the difference between the real value and the measured value in the debonding region. Table 1 shows the calculated results of FMCW images for Sample 1 and Sample 2. The mean level of detection error is about

FIGURE 15. Results processed by the proposed method on FMCW images. (a) Sample 1. (b) Sample 2.

TABLE 1. Detection results of FMCW images for sample 1 and sample 2.

Object	Sample 1			Sample 2		
Metric	Real area （mm²）	Measured area （mm²）	Error （%）	Real area （mm²）	Measured area （mm²）	Error （%）
Defect-I	1627.93	1507.83	7.38	1758.69	1593.45	9.40
Defect-II	263.48	249.37	5.36	124.26	137.15	10.37
Defect-III	129.71	147.21	13.49	97.83	110.64	13.09
Defect-IV	104.36	112.46	7.76	81.54	90.59	11.10
Defect-V	92.12	79.28	13.94	30.27	34.57	14.21
Defect-VI	56.29	64.39	14.39	20.93	22.04	5.30
Defect-VII	32.73	37.54	14.70	13.49	14.46	7.19
Defect-VIII	24.49	27.71	13.15	7.21	7.98	10.68
Mean Error	11.27%			10.17%		

10.17%-11.27%. The proposed method provides new ideas and methods for quantitative analysis of FMCW detection.

V. CONCLUSION

In order to improve the detection ability of debonds in layered structures, a new method is proposed, which can ensure quantitative analysis as accurate as possible without losing the positioning accuracy. TPS detection was used to validate this method. By using multi-directional structural elements for measuring differences between the target and local surroundings, the multi-directional mathematical morphological filter is constructed, which can greatly highlight defective edges and suppress clutters. In addition, the improved Otsu method can extract the defective edge well and obtain superior detection results. Finally, through comparative experiments and quantitative analysis, it is demonstrated that the proposed method can efficiently extract edges of low SNR images, and control the detection error of the debonding region within 10.17%-11.27%. We also found that the error can be controlled through scanning accuracy, material and size of lens, etc. In the future, we will consider more factors for reducing the detection errors. The proposed method is also suitable for extracting the edges of other low-quality images.

REFERENCES

[1] D.-D. Zhang, J.-J. Ren, J. Gu, L.-J. Li, J.-Y. Zhang, W.-H. Xiong, Y.-F. Zhong, and T.-Y. Zhou, "Nondestructive testing of bonding defects in multilayered ceramic matrix composites using THz time domain spectroscopy and imaging," *Compos. Struct.*, vol. 251, Nov. 2020, Art. no. 112624.

[2] S. Costil, S. Lukat, P. Bertrand, C. Langlade, and C. Coddet, "Surface treatment effects on ceramic matrix composites: Case of a thermal sprayed alumina coating on SiC composites," *Surf. Coat. Technol.*, vol. 205, no. 4, pp. 1047–1054, Nov. 2010.

[3] J. Ren, L. Li, D. Zhang, X. Qiao, Q. Lv, and G. Gao, "Study on intelligent recognition detection technology of debond defects for ceramic matrix composites based on terahertz time domain spectroscopy," *Appl. Opt.*, vol. 55, no. 26, pp. 7204–7211, 2016.

[4] E. Cristofani, F. Friederich, S. Wohnsiedler, C. Matheis, J. Jonuscheit, M. Vandewal, and R. Beigang, "Nondestructive testing potential evaluation of a terahertz frequency-modulated continuous-wave imager for composite materials inspection," *Opt. Eng.*, vol. 53, no. 3, Mar. 2014, Art. no. 031211.

[5] B. Dai, P. Wang, T.-Y. Wang, C.-W. You, Z.-G. Yang, K.-J. Wang, and J.-S. Liu, "Improved terahertz nondestructive detection of debonds locating in layered structures based on wavelet transform," *Compos. Struct.*, vol. 168, pp. 562–568, May 2017.

[6] C. D. Stoik, M. J. Bohn, and J. L. Blackshire, "Nondestructive evaluation of aircraft composites using transmissive terahertz time domain spectroscopy," *Opt. Exp.*, vol. 16, no. 21, pp. 17039–17051, Oct. 2008.

[7] C.-H. Ryu, S.-H. Park, D.-H. Kim, K.-Y. Jhang, and H.-S. Kim, "Nondestructive evaluation of hidden multi-delamination in a glass-fiber-reinforced plastic composite using terahertz spectroscopy," *Compos. Struct.*, vol. 156, pp. 338–347, Nov. 2016.

[8] N. Palka, R. Panowicz, M. Chalimoniuk, and R. Beigang, "Non-destructive evaluation of puncture region in polyethylene composite by terahertz and X-ray radiation," *Compos. B, Eng.*, vol. 92, pp. 315–325, May 2016.

[9] D. Giovannacci, H. C. Cheung, G. C. Walker, J. W. Bowen, D. Martos-Levif, D. Brissaud, L. Cristofol, and Y. Mélinge, "Time-domain imaging system in the terahertz range for immovable cultural heritage materials," *Strain*, vol. 55, no. 2, Apr. 2019, Art. no. e12292.

[10] G. Yan, A. Markov, Y. Chinifooroshan, S. Tripayhi, W.-J. Bock, and M. Skorobogatiy, "Resonant THz sensor for paper quality monitoring using THz fiber Bragg gratings," *Opt. Lett.*, vol. 38, no. 13, pp. 2200–2202, Jul. 2013.

[11] W. Tribe, D. Newnham, P. Taday, and M. Kemp, "Hidden object detection: Security applications of terahertz technology," *Proc. SPIE*, vol. 5354, pp. 168–176, Apr. 2004.

[12] T. Zhang, H. Huang, Z. Zhang, H. Gao, L. Gao, and Z. Zheng, "Sensitive characterizations of polyvinyl chloride using terahertz time-domain spectroscopy," *Infr. Phys. Technol.*, vol. 118, Nov. 2021, Art. no. 103878.

[13] J. Federici and L. Moeller, "Review of terahertz and subterahertz wireless communications," *J. Appl. Phys.*, vol. 107, no. 11, Jun. 2010, Art. no. 111101.

[14] K. Cooper, R. Dengler, N. Llombart, T. Bryllert, G. Chattopadhyay, E. Schlecht, J. Gill, C. Lee, A. Skalare, and I. Mehdi, "Penetrating 3-D imaging at 4- and 25-m range using a submillimeter-wave radar," *IEEE Trans. Microw. Theory Techn.*, vol. 56, no. 12, pp. 2771–2778, Dec. 2008.

[15] I. F. Akyildiz, J. M. Jornet, and C. Han, "Terahertz band: Next frontier for wireless communications," *Phys. Commun.*, vol. 12, pp. 16–32, Sep. 2014.

[16] D. Crawley, S. Withington, and J. Obradovic, "Area-scan camera for terahertz holography," *Rev. Sci. Instrum.*, vol. 77, no. 5, May 2006, Art. no. 053106.

[17] K. Ahi, S. Shahbazmohamadi, and N. Asadizanjani, "Quality control and authentication of packaged integrated circuits using enhanced-spatial-resolution terahertz time-domain spectroscopy and imaging," *Opt. Lasers Eng.*, vol. 104, pp. 274–284, May 2018.

[18] H. Liu, Z. Zhang, X. Zhang, Y. Yang, Z. Zhang, X. Liu, F. Wang, Y. Han, and C. Zhang, "Dimensionality reduction for identification of hepatic tumor samples based on terahertz time-domain spectroscopy," *IEEE Trans. Terahertz Sci. Technol.*, vol. 8, no. 3, pp. 271–277, May 2018.

[19] G. Rubio-Cidre, A. Badolato, L. Úbeda-Medina, J. Grajal, B. Mencia-Oliva, and B.-P. Dorta-Naranjo, "DDS-based signal-generation architecture comparison for an imaging radar at 300 GHz," *IEEE Trans. Instrum. Meas.*, vol. 64, no. 11, pp. 3085–3098, Nov. 2015.

[20] J. B. Perraud, A. F. Obaton, J. Bou-Sleiman, B. Recur, H. Balacey, F. Darracq, J.-P. Guillet, and P. Mounaix, "Terahertz imaging and tomography as efficient instruments for testing polymer additive manufacturing objects," *Appl. Opt.*, vol. 55, no. 13, pp. 3462–3467, 2016.

[21] L. Minkeviius, D. Jokubauskis, I. Kaalynas, S. Orlov, A. Urbas, and G. Valušis, "Bessel terahertz imaging with enhanced contrast realized by silicon multi-phase diffractive optics," *Opt. Exp.*, vol. 27, no. 25, pp. 36358–36367, Nov. 2019.

[22] J.-B. Perraud, J.-P. Guillet, O. Redon, M. Hamdi, F. Simoens, and P. Mounaix, "Shape-from-focus for real-time terahertz 3D imaging," *Opt. Lett.*, vol. 44, no. 3, pp. 483–486, 2019.

[23] W. Zhen, X. Wang, W. Sun, S. Feng, P. Han, J. Ye, Y. Yue, and Y. Zhang, "Vectorial diffraction properties of THz vortex Bessel beams," *Opt. Exp.*, vol. 26, no. 2, pp. 1506–1520, Jan. 2018.

[24] L. Niu, K. Wang, Y. Yang, Q. Wu, X. Ye, Z. Yang, J. Liu, and H. Yu, "Diffractive elements for zero-order Bessel beam generation with application in the terahertz reflection imaging," *IEEE Photon. J.*, vol. 11, no. 1, pp. 1–12, Feb. 2019.

[25] F. Ellrich, M. Bauer, N. Schreiner, A. Keil, and T. Pfeiffer, "Terahertz quality inspection for automotive and aviation industries," *J. Infr., Millim., Terahertz Waves*, vol. 41, no. 4, pp. 470–489, Apr. 2020.

[26] M. Caris, S. Stanko, A. Wahlen, R. Sommer, J. Wilcke, N. Pohl, A. Leuther, and A. Tessmann, "Very high resolution radar at 300 GHz," in *Proc. 11th Eur. Radar Conf.*, Rome, Italy, Oct. 2014, pp. 494–496.

[27] W. Hu, Y. Li, Z. Han, and J. Ni, "High-resolution range profile reconstruction method for terahertz FMCW radar," *Appl. Opt.*, vol. 60, no. 22, pp. 6400–6408, Jul. 2021.

[28] N. S. Schreiner, W. Sauer-Greff, R. Urbansky, G. V. Freymann, and F. Friederich, "Multilayer thickness measurements below the Rayleigh limit using FMCW millimeter and terahertz waves," *Sensors*, vol. 19, no. 18, pp. 3910–3912, Sep. 2019.

[29] P. Gulden, M. Vossiek, E. Storck, and P. Heide, "Application of state space frequency estimation techniques to radar systems," in *Proc. IEEE Int. Conf. Acoust., Speech, Signal Process.*, May 2001, pp. 2877–2880.

[30] M. Testar and R. Stirling-Gallacher, "New super-resolution ranging technique for FMCW radar systems," *Proc. SPIE*, vol. 8188, no. 1, Oct. 2011, Art. no. 81880K.

[31] M. Pauli, B. Gottel, S. Scherr, A. Bhutani, S. Ayhan, W. Winkler, and T. Zwick, "Miniaturized millimeter-wave radar sensor for high-accuracy applications," *IEEE Trans. Microw. Theory Techn.*, vol. 65, no. 5, pp. 1707–1715, May 2017.

[32] T. M. Wong, M. Kahl, P. Haring Bolívar, and A. Kolb, "Computational image enhancement for frequency modulated continuous wave (FMCW) THz image," *J. Infr., Millim., Terahertz Waves*, vol. 40, no. 7, pp. 775–800, Jul. 2019.

[33] X. Bai and F. Zhou, "Analysis of new top-hat transformation and the application for infrared dim small target detection," *Pattern Recognit.*, vol. 43, no. 6, pp. 2145–2156, 2010.

[34] C. Yuan, Z. Xiong, X. Zhou, and X. Peng, "Study of infrared image edge detection based on Sobel operator," *Laser Infr.*, vol. 39, no. 1, pp. 85–87, Jan. 2009.

[35] M. Kang and Q. Xu, "Adaptive edge-detection method based on Prewitt algorithm," *Appl. Res. Comput.*, vol. 26, no. 6, pp. 2383–2386, Jun. 2009.

[36] M. Kang, Q. Xu, and B. Wang, "A Roberts' adaptive edge detection method," *J. Xi'an Jiaotong Univ.*, vol. 42, no. 10, pp. 1240–1244, Oct. 2008.

[37] X. Soria, E. Riba, and A. Sappa, "Dense extreme inception network: Towards a robust CNN model for edge detection," in *Proc. IEEE Winter Conf. Appl. Comput. Vis. (WACV)*, Mar. 2020, pp. 1923–1932.

[38] S. Xie and Z. Tu, "Holistically-nested edge detection," in *Proc. IEEE Int. Conf. Comput. Vis. (ICCV)*, Dec. 2015, pp. 1395–1403.

[39] Z. Su, W. Liu, Z. Yu, D. Hu, Q. Liao, Q. Tian, M. Pietikainen, and L. Liu, "Pixel difference networks for efficient edge detection," in *Proc. IEEE/CVF Int. Conf. Comput. Vis. (ICCV)*, Oct. 2021, pp. 5097–5107.

[40] M. Pu, Y. Huang, Q. Guan, and H. Ling, "RINDNet: Edge detection for discontinuity in reflectance, illumination, normal and depth," in *Proc. IEEE/CVF Int. Conf. Comput. Vis. (ICCV)*, Oct. 2021, pp. 6859–6868.

WENNA ZHANG received the B.S. and M.S. degrees in information and communication engineering from the North University of China, Taiyuan, China, where he is currently pursuing the Ph.D. degree with the School of Information and Communication Engineering. His main research interests include signal processing, wireless communication, and automatic modulation recognition.

JIALIN SONG received the B.S. and M.S. degrees in information and communication engineering from the North University of China, Taiyuan, China, where he is currently pursuing the Ph.D. degree with the School of Information and Communication Engineering. His main research interests include deep learning and image processing.

ZHAOBA WANG received the Ph.D. degree in instruments science and technology from the Nanjing University of Science and Technology, in 2002. He is currently a Professor with the School of Information and Communication Engineering, North University of China. His main research interests include information processing and reconstruction, computer vision, and image processing.

KAILIANG XUE received the B.S. and M.S. degrees in information and communication engineering from the North University of China, Taiyuan, China, where he is currently pursuing the Ph.D. degree with the School of Information and Communication Engineering. His main research interests include terahertz non-destructive testing, signal processing, and computational imaging.

YONG JIN received the Ph.D. degree from the North University of China, in 2013. He is currently a Professor with the School of Information and Communication Engineering, North University of China. His research interests include image processing, online inspections, and big data analytics.

YOUXING CHEN received the Ph.D. degree from the North University of China, in 2010. He is currently a Professor with the School of Information and Communication Engineering, North University of China. His research interests include image processing, signal processing, and non-destructive testing.

XIN GUO received the Ph.D. degree from Lanzhou University, in 2019. She is currently a Lecturer with the School of Information and Communication Engineering, North University of China. Her research interests include nanomaterials and electric photonic detector, sectors image processing, and non-destructive testing.

• • •